

## Proton Transfer in Nanoconfined Polar Solvents. II. Adiabatic Proton Transfer Dynamics

Ward H. Thompson\*

Department of Chemistry, University of Kansas, Lawrence, Kansas 66045

Received: June 7, 2005

The reaction dynamics for a model phenol–amine proton transfer system in a confined methyl chloride solvent have been simulated by mixed quantum–classical molecular dynamics. In this approach, the proton vibration is treated quantum mechanically (and adiabatically), while the rest of the system is described classically. Nonequilibrium trajectories are used to determine the proton transfer reaction rate constant. The reaction complex and methyl chloride solvent are confined in a smooth, hydrophobic spherical cavity, and radii of 10, 12, and 15 Å have been considered. The effects of the cavity radius and the heavy atom (hydrogen bond) distance on the reaction dynamics are considered, and the mechanism of the proton transfer is examined in detail by analysis of the trajectories.

### 1. Introduction

It is now possible to synthesize nanostructured porous materials with a tremendous variety of properties including sol–gels,<sup>1</sup> zeolites, organic and inorganic supramolecular assemblies,<sup>2–4</sup> reverse micelles,<sup>5</sup> vesicles, and even proteins.<sup>6</sup> The interest in these materials derives from their potential for carrying out useful chemistry (e.g., as microporous and mesoporous catalysts with critical specificity, fuel cell electrodes and membranes, molecular sieves, and chemical sensors) and for understanding the chemistry in similar systems found in nature.<sup>7</sup> Despite the advances in synthetic techniques, our understanding of chemistry in solvents confined in nanometer-size cavities and pores is still relatively limited.<sup>8–41</sup> Ultimately, one would like to design nanostructured materials adapted for specific chemical purposes, e.g., catalysis or sensing, by controlling the cavity/pore size, geometry, and surface chemistry. To develop guidelines for this design, we must first understand how the characteristics of the confining framework affect the chemistry. These effects are particularly pronounced when the chemical process of interest involves charge transfer,<sup>16–41</sup> e.g., proton or electron transfer, and is therefore intimately coupled to the solvent dynamics.<sup>42–44</sup> Theoretical and simulation approaches can be particularly powerful in this context, since the properties of the confining framework can be straightforwardly controlled and systematically varied, isolating their effects.

In this paper, we present vibrationally adiabatic mixed quantum–classical molecular dynamics simulations of a model phenol–amine proton transfer reaction in a nanoconfined methyl chloride solvent (in a spherical hydrophobic cavity). We have previously studied this system using Monte Carlo simulations to investigate the distribution of reaction complex positions in the cavity and the reaction free energies.<sup>30</sup> The key results of those Monte Carlo simulations were as follows: (1) The reactant proton transfer complex is located near the cavity wall, while the product complex is found primarily in the interior. (2) The reaction free energy depends strongly on the reaction complex position varying from endothermic (by  $\sim 1$  kcal/mol) near the cavity wall to exothermic (by  $\sim 5$  kcal/mol) deep in the cavity interior. Together, these demonstrate that the reaction coordinate must involve motion of the reaction complex from near the cavity wall to the interior. However, the results did not allow

us to determine the precise nature of the mechanism, for example, whether the motion of the reaction complex follows or precedes the solvent reorganization (which constitutes the reaction coordinate in a bulk solvent).<sup>42–44</sup> In the present work, we address this issue in addition to calculating proton transfer reaction rate constants. We also examine the effect of cavity size and heavy atom (O $\cdots$ N) distance on the dynamics.

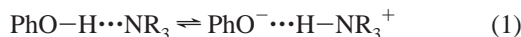
There have been a number of experimental studies of proton transfer in solvents confined in sol–gels<sup>32–35</sup> and reverse micelles,<sup>36–41</sup> several in just the past few years.<sup>33–38</sup> In addition, significant attention has been devoted to developing supramolecular assemblies that can function as catalysts.<sup>2–4</sup> To our knowledge, our recent work is the first theoretical study of proton transfer in a nanoconfined solvent.<sup>30</sup> Experimental studies have found significant differences in the proton transfer reaction dynamics in reverse micelles and sol–gels as compared to bulk solvent, as evidenced by slower solvation dynamics and lower reaction rate constants. (Two exceptions are the recent work by Kwon and Jang<sup>38</sup> and proton diffusion rates in sol–gels in which the low water content in the larger pores limits the transport.<sup>32,34</sup>) However, alterations of the reaction mechanism and the effects of surface chemistry, confining framework geometry, and counterion effects have not been systematically explored.

The spherical hydrophobic nanocavities considered here are among the simplest model confining frameworks. While they do not explicitly model a particular experimental system, they can provide important insights into chemistry occurring in a diverse range of nanoscale confining frameworks. In particular, the simplicity of the interactions serves to isolate the effects of confinement. Thus, studies of chemistry in these simple cavities serves as a baseline with which confinement frameworks with more complex geometries and surface chemistries can be compared. In this way, these spherical nanocavities represent a starting point for systematic studies of confining framework properties. They thereby also assist in developing a general, fundamental understanding that spans a variety of systems (i.e., in identifying unifying principles of confinement effects). Finally, chemistry in these hydrophobic cavities displays rich, interesting features that are not always as simple as the underlying model.

The remainder of the paper is organized as follows. The reaction complex, solvent, and confining nanoscale spherical hydrophobic cavity are discussed in section 2. The details of the mixed quantum–classical molecular dynamics simulations are described in section 3, and the results are presented in section 4. A discussion of the calculated rate constants, reaction free energies, and observed mechanisms is offered in section 5. Finally, some concluding remarks are given in section 6.

## 2. System

The details of the proton transfer reaction complex, CH<sub>3</sub>Cl solvent, and cavity models are provided elsewhere.<sup>30</sup> Briefly, the reaction complex is a simplified model of a phenol–amine proton transfer reaction



originally developed by Borgis.<sup>45–47</sup> The present work uses a two valence bond (VB) state model<sup>44</sup> to account for the changes in the reaction complex electronic structure in response to solvent motions instead of switching functions.<sup>45</sup> In the present calculations, the O–H–N angle is constrained to be linear, and the heavy atom (O $\cdots$ N) distance is held fixed during each simulation so this is effectively an intramolecular proton transfer reaction. In addition, the gas-phase reaction endothermicity has been modified so that the reaction in the nanocavities considered here is approximately thermoneutral. The solute and methyl chloride solvent molecules<sup>48</sup> interact through Lennard-Jones and Coulomb potentials. The Lennard-Jones parameters for the solute and solvent and the charges for the solvent and the two solute VB states are given in ref 30.

A model potential is used for the cavity in which the interactions of the solute and solvent molecules with the cavity wall involve only a Lennard-Jones term integrated over a continuous material surrounding the spherical cavity.<sup>8,9,26</sup> The result is a potential energy that depends only on the distance of each interaction site in a molecule from the center of the cavity. In this work, the cavity radius,  $R_{\text{cav}}$ , is taken to be 10, 12, and 15 Å. The density of the solution inside the cavity is kept approximately the same for these cavity sizes ( $\rho = 0.8 \text{ g/cm}^3$ ). Note that the actual densities may be slightly different than these nominal densities, since for a fixed cavity size, it is not possible to attain an arbitrary density.<sup>49</sup> Because of the spherical symmetry of the cavity, structural properties of molecules need only be examined as a function of radial coordinates.

## 3. Mixed Quantum–Classical Molecular Dynamics Simulations

While our previous Monte Carlo simulation results suggest that this proton transfer system is in the (vibrationally) nonadiabatic regime, in this paper we examine only the adiabatic dynamics that provide a first look at mechanistic information and an important point of comparison with nonadiabatic dynamics that we will present elsewhere. (Adiabatic mixed quantum–classical simulations have previously been used to investigate proton transfer.<sup>46,50,51</sup>) Here, the proton vibration (in one dimension) is treated quantum mechanically, while the rest of the solute and solvent degrees of freedom are described classically. Thus, the system evolves under the classical Hamiltonian

$$H_n(\mathbf{P}, \mathbf{Q}, \mathbf{p}_e, \mathbf{e}) = \sum_i \frac{\mathbf{P}_i^2}{2m_i} + \sum_i \frac{\mathbf{p}_{e,i}^2}{2I_i} + E_n(\mathbf{Q}, \mathbf{e}) \quad (2)$$

where  $\mathbf{P}_i$  is the center-of-mass momentum of molecule  $i$  (including the solute reaction complex) conjugate to coordinate  $\mathbf{Q}_i$ ,  $\mathbf{p}_{e,i}$  is the orientational momentum of molecule  $i$  conjugate to the unit vector coordinate  $\mathbf{e}_i$ , and  $I_i$  is the moment of inertia of molecule  $i$ . Here,  $E_n(\mathbf{Q}, \mathbf{e})$  is the (proton) vibrationally adiabatic energy level obtained by solving the vibrational Schrödinger equation

$$\hat{h}_r(\mathbf{Q}, \mathbf{e}) \phi_n(r; \mathbf{Q}, \mathbf{e}) = E_n(\mathbf{Q}, \mathbf{e}) \phi_n(r; \mathbf{Q}, \mathbf{e}) \quad (3)$$

The vibrational Hamiltonian is given by

$$\hat{h}_r(\mathbf{Q}, \mathbf{e}) = \frac{\hat{p}_r^2}{2m_H} + V_g(r, \mathbf{Q}, \mathbf{e}) \quad (4)$$

where  $r$  is the O–H distance and  $V_g(r, \mathbf{Q}, \mathbf{e})$  is the total electronic ground-state potential energy of the system. It is assumed that the reaction complex moment of inertia is independent of the proton position,  $r$ . The Schrödinger equation, eq 3, is solved at every time step in the molecular dynamics simulation.

In the present calculations, a sinc-function discrete variable representation (DVR) basis<sup>52</sup> with a potential cutoff of 4 eV was used with a grid spacing of  $\Delta r = 0.032 \text{ Å}$ . The number of DVR grid points ranged from 43 to 49 (depending on  $R_{\text{O–N}}$  and the proton potential used for the potential cutoff truncation). The Schrödinger equation, eq 3, was solved using the Lanczos algorithm<sup>53</sup> in which only the three lowest vibrational states of the proton were converged. The starting vector for the Lanczos algorithm at time  $t$  was taken to be a linear combination (with equal coefficients) of the three eigenstates obtained at  $t - \Delta t$ .<sup>54</sup>

The vibrationally adiabatic proton transfer reaction dynamics are simulated using nonequilibrium trajectories. Specifically, the system is equilibrated with an umbrella potential

$$V_{\text{umb}}(\mathbf{Q}, \mathbf{e}) = \frac{1}{2} k_{\text{umb}} [\Delta E(\mathbf{Q}, \mathbf{e}) - \Delta E_0]^2 \quad (5)$$

added to the physical potential to constrain the complex to be reactants. Here,  $\Delta E$  is the solvent coordinate defined as

$$\Delta E(\mathbf{Q}, \mathbf{e}) = V_g(r_R, \mathbf{Q}, \mathbf{e}) - V_g(r_P, \mathbf{Q}, \mathbf{e}), \quad (6)$$

$\Delta E_0$  is a value characteristic of reactants, and  $r_R$  and  $r_P$  are values of the O–H distance characteristic of the reactants and products, respectively. In these simulations,  $\Delta E_0 = -8 \text{ kcal/mol}$ ,  $k_{\text{umb}} = 0.1 \text{ (kcal/mol)}^{-1}$ ,  $r_R = 0.95 \text{ Å}$ , and  $r_P = R_{\text{O–H}} - 0.9 \text{ Å}$ ; we have verified that the results are not sensitive to these choices. The equilibration with an umbrella potential is carried out first with purely classical dynamics, followed by a mixed quantum–classical equilibration period. Following the equilibration, the umbrella potential is removed and the subsequent reaction dynamics monitored. The initial conditions for the nonequilibrium trajectories are changed by varying the duration of both the classical (between 0.3 and 1.15 ns) and mixed quantum–classical (between 0.1 and 0.3 ns) equilibration periods. The results presented are obtained from ensembles of 180 (for the  $R_{\text{O–H}} = 2.7 \text{ Å}$  simulations) or 120 (for all other cases) nonequilibrium trajectories, each of length 500 ps.

The average temperature during the simulations is  $\sim 265 \text{ K}$  maintained using a Nosé–Poincaré thermostat,<sup>55</sup> and all simulations are carried out with a solution density of  $\sim 0.8 \text{ g/cm}^3$ ; this density gives  $N_{\text{mol}} = 26, 49$ , and 103 for  $R_{\text{cav}} = 10, 12$ , and 15

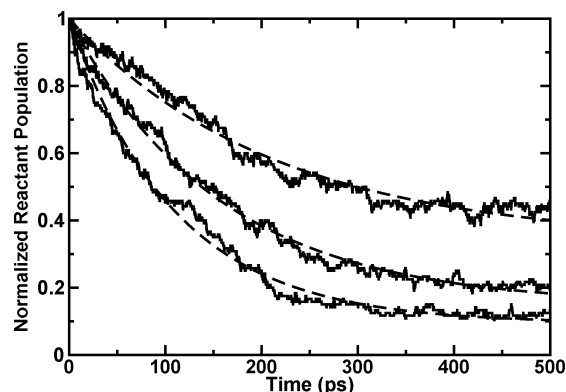


**Figure 1.** The normalized reactant population of the proton transfer complex with  $R_{O-N} = 2.6$  Å is plotted as a function of time as obtained from nonequilibrium mixed quantum–classical trajectories. Results are presented as solid lines, from top to bottom, for  $R_{cav} = 10, 12$ , and  $15$  Å. The best fits of eq 7 to the data are also shown as dashed lines.

**TABLE 1: Parameters  $P_R^{eq}$  and  $\tau$  Obtained from Fitting the Reactant Population as a Function of Time to Eq 7<sup>a</sup>**

$R_{cav}$ (Å)	$R_{OH}$ (Å)	$P_R^{eq}$	$\tau$ (ps)	$k_f$ (ns <sup>-1</sup> )	$k_b$ (ns <sup>-1</sup> )	$\Delta G_{rxn}$ (kcal/mol)
10	2.6	0.34	212	3.1	1.6	-0.33
10	2.7	0.07	98	9.5	0.70	-1.3
10	2.8	0.02	59	17	0.34	-1.9
12	2.6	0.15	156	5.5	0.96	-0.87
12	2.7	0.04	77	13	0.46	-1.6
12	2.8	0.007	46	22	0.16	-2.4
15	2.6	0.09	110	8.2	0.85	-1.1
15	2.7	0.02	61	16	0.34	-1.9
15	2.8	0.004	38	27	0.12	-2.7

<sup>a</sup> The forward and backward rate constants and free energy of reaction calculated from the fit parameters are also presented.

Å, respectively. The time step in the simulations was  $\Delta t = 1$  fs.

#### 4. Results

The proton transfer reaction dynamics of the model phenol–amine proton transfer system have been simulated in smooth hydrophobic cavities of radii 10, 12, and 15 Å with hydrogen bond (O–N or “heavy atom”) distances of 2.6, 2.7, and 2.8 Å. The results of these calculations for  $R_{O-N} = 2.6$  Å for cavities of different sizes are shown in Figure 1. Specifically, the (normalized) time-dependent reactant populations are shown as a function of time averaged over 120 nonequilibrium trajectories. The data are fit well by a single exponential of the form

$$P_R(t) = (1 - P_R^{eq}) e^{-t/\tau} + P_R^{eq} \quad (7)$$

where  $P_R(t)$  is the time-dependent reactant population and  $P_R^{eq}$  is the equilibrium (or long-time) population. The fits to the data are shown in Figure 1, and the fit parameters are given in Table 1. Here, the reactant population is defined by the value of the solvent coordinate, eq 6. Namely, the reactant population at time  $t$  is given by

$$P_R(t) = \langle \theta[-\Delta E(Q(t), \mathbf{e}(t))] \rangle, \quad (8)$$

where  $\theta(x)$  is the Heaviside step function. It is clear from these results that as  $R_{cav}$  is increased the proton transfer reaction rate constant increases. At the same time, the equilibrium population of the reactants decreases, indicating a more exothermic reaction (see section 5).

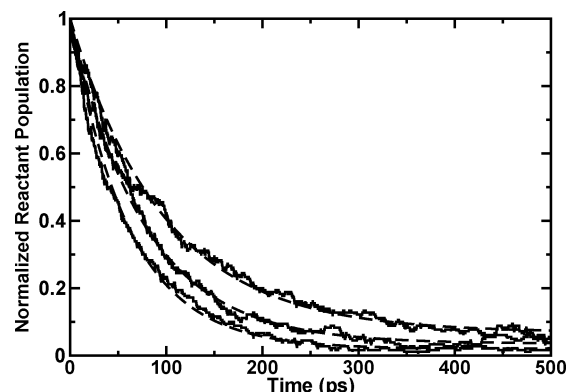


**Figure 2.** Same as Figure 1, but with  $R_{O-N} = 2.7$  Å, and in this case, results from 180 trajectories are presented.

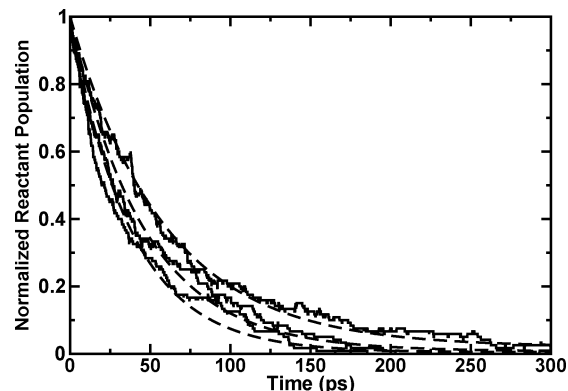
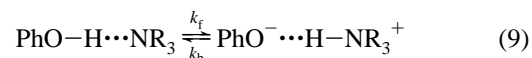


**Figure 3.** Same as Figure 1, but with  $R_{O-N} = 2.8$  Å.

We have analyzed the nonequilibrium trajectory results presented in section 4 by assuming that the reaction kinetics are of the form



With the initial conditions  $[\text{PhO}-\text{H} \cdots \text{NR}_3]_0 = 1$  and  $[\text{PhO}^- \cdots \text{H}-\text{NR}_3^+]_0 = 0$  imposed in the nonequilibrium simulations, the solution to the rate equations is<sup>56</sup>

$$[\text{PhO}-\text{H} \cdots \text{NR}_3]_t = \left(1 - \frac{1}{1+K}\right) e^{-(k_f+k_b)t} + \frac{1}{1+K} \quad (10)$$

where  $K = k_f/k_b$  is the equilibrium constant for the proton transfer reaction. Thus, our fit to the time-dependent reactant population, eq 7, gives  $\tau = 1/(k_f + k_b)$  and  $P_R^{eq} = 1/(1 + K)$ . This allows us to obtain  $k_f$ ,  $k_b$ , and  $K$ . Further, the reaction free energy can be extracted from

$$K = e^{-\Delta G_{rxn}/k_B T} \quad (11)$$

where  $k_B$  is Boltzmann’s constant. The forward and backward rate constants and  $\Delta G_{rxn}$  obtained in this way are listed in Table 1.

Results for a larger O–N distance,  $R_{O-N} = 2.7$  Å, are shown in Figure 2 for the three cavity sizes. Finally, the normalized reactant population is plotted in Figure 3 for  $R_{O-N} = 2.8$  Å for  $R_{cav} = 10, 12$ , and  $15$  Å as a function of time. We can clearly see that the rate constant increases as the cavity radius is increased for all values of  $R_{O-N}$ . In addition, these results show that for all values of  $R_{O-N}$  the decay constant  $\tau$  and the forward reaction rate constant  $k_f$  grow larger as the cavity size is increased. The fits to the data according to eq 7 also indicate

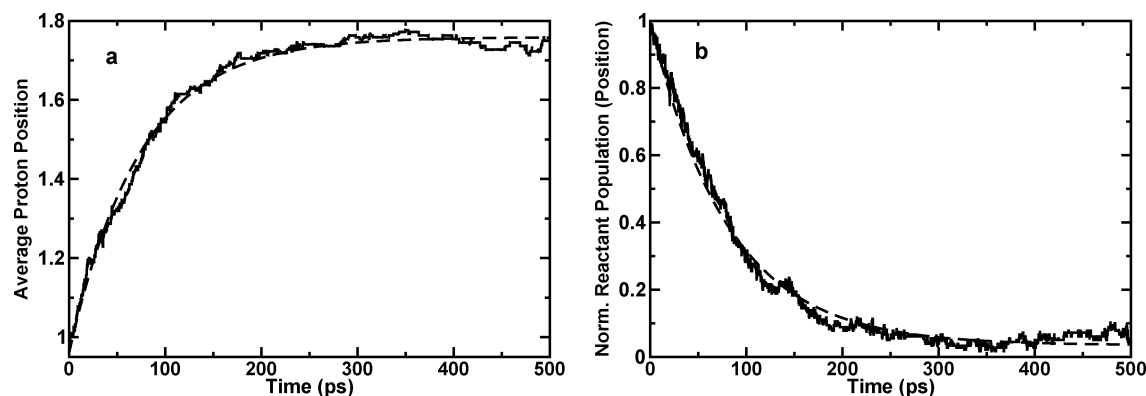


**Figure 4.** Results for the reaction dynamics are shown using alternative approaches to monitoring the reaction progress for  $R_{\text{cav}} = 12 \text{ \AA}$  and  $R_{\text{O-N}} = 2.7 \text{ \AA}$ . Specifically, (a) the average proton position and (b) the normalized reactant population based on the reaction complex position, eq 12, are plotted vs time.

that the equilibrium population decreases as  $R_{\text{cav}}$  increases (see Table 1). (However, we note that, when the equilibrium constant is very small, there is greater uncertainty in this result.) Further, for a fixed cavity size, the forward rate constant increases, and the reaction becomes more exothermic as the O–N distance increases. This is due to the increasing dipole moment for the products of the proton transfer reaction as  $R_{\text{O-N}}$  is made larger. This is a dramatic effect as the forward rate constant changes by a factor of  $\sim 3$ – $5$  and the reaction free energy by  $\sim 1.5 \text{ kcal/mol}$ .

In Figures 1–3, we have used the solvent coordinate defined in eq 6 to determine the reactant populations. However, this is not the only possible choice. We could instead have used the proton position (i.e.,  $\langle \hat{r} \rangle$ ) or, on the basis of the results of our previous Monte Carlo studies,<sup>30</sup> the reaction complex position in the cavity. In Figure 4, we show the results obtained using these alternative choices for following the reaction. In particular, the average proton position (an ensemble average of the quantum expectation value) is plotted as a function of time in Figure 4a, and the reactant population based on the complex position is shown in Figure 4b for the case of the  $12 \text{ \AA}$  cavity with  $R_{\text{O-N}} = 2.7 \text{ \AA}$ .<sup>57</sup> In the latter, the reactant population is given by

$$P_{\text{R}}^{\text{pos}}(t) = \langle \theta[R_{\text{cm}}(t) - R_{\text{div}}] \rangle \quad (12)$$

where  $R_{\text{cm}}$  is the center-of-mass of the reaction complex and  $R_{\text{div}}$  is a radial position that divides reactants and products. The results can be well-fit with a single exponential (also shown). In both cases, the time constant and long-time value agree well with those obtained using the solvent coordinate to define the reactants in Figure 2 and Table 1. Specifically, the time constants in the exponential fits to the average proton position and complex position-based population are 74 and 81 ps, respectively, compared with  $\tau = 77 \text{ ps}$  for the solvent coordinate-based population. The equilibrium (long-time) populations obtained in the fits are 0.023, 0.034, and 0.036 for the proton position, complex position-based population, and the solvent coordinate-based population, respectively. (These three approaches thus give forward rate constants in the range  $11.9$ – $13.3 \text{ ns}^{-1}$  and reaction free energies between  $-1.64$  and  $-1.86 \text{ kcal/mol}$ .)

## 5. Discussion

**5.1. Mechanisms.** Our previous Monte Carlo simulations on the same phenol–amine system considered here showed that the position of the proton transfer reaction complex was part of the reaction coordinate. In particular, we found that (1) the

reactants are preferentially found next to the cavity wall, while the products are found almost exclusively fully solvated in the cavity interior; and (2) the products are not stable near the cavity wall, and the reactants are not stable in the cavity interior. The mechanism for the proton transfer reaction was not established, however. Namely, one can envision at least three potential mechanisms for the reaction from reactants to products: (1) The solvent rearranges first, followed by movement of the reaction complex to the cavity interior. (2) The reaction complex first diffuses into the cavity interior and then the solvent reorganizes to form products. (3) The solvent reorganization and reaction complex motion are concerted. By simulating the mixed quantum–classical dynamics, we can address the question of which mechanisms are operative, at least in the vibrationally adiabatic limit (which provides an interesting comparison with the nonadiabatic dynamics currently under study). As we now discuss, all three possible mechanisms are, in fact, observed.

A simple approach for visualizing the reaction mechanism is to plot individual nonequilibrium trajectories in two coordinates: the solvent coordinate,  $\Delta E$ , given in eq 6, and the reaction complex position (given by its center-of-mass). The reactions considered here involve relatively low barriers, so the trajectories can exhibit significant recrossing of reactant–product dividing surfaces (both in the solvent coordinate and complex position); we will return to this issue below. However, for many trajectories, the mechanism can be readily identified by inspection. In Figure 5, we show trajectories (for  $R_{\text{O-N}} = 2.7 \text{ \AA}$  and  $R_{\text{cav}} = 10 \text{ \AA}$ ) that demonstrate the occurrence of each of the three possible mechanisms discussed above. The trajectories are all initiated as reactants with  $\Delta E < 0$  and the reaction complex center-of-mass around  $7 \text{ \AA}$  from the cavity center. In the first trajectory (left panel), the reactant–product dividing surface in the solvent coordinate is crossed first (i.e., the solvent reorganizes to stabilize the product complex), and the reaction complex then moves relatively rapidly into the cavity interior where it is more stable.<sup>30</sup> As discussed below, this mechanism is the dominant one for the systems studied here. The second trajectory (center panel) first crosses the solvent coordinate dividing surface but returns to reactants before the reaction complex diffuses into the interior. The proton transfer reaction is then completed by the second mechanism: The reaction complex diffuses into the cavity interior (to  $\sim 3 \text{ \AA}$  from the center) where the solvent reorganizes rapidly to form the products (this last step is significantly downhill in free energy<sup>30</sup>). Finally, a concerted mechanism is illustrated (right panel) in which the solvent reorganizes and the reaction complex moves at the same



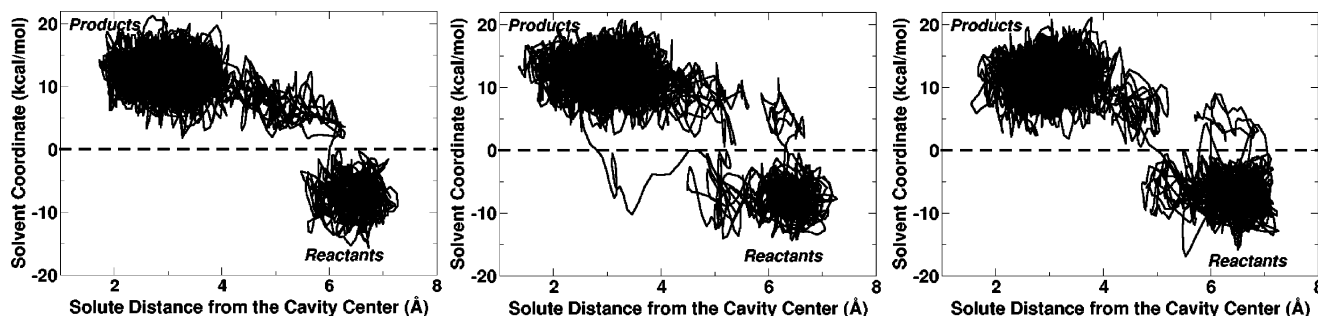


**Figure 5.** Selected vibrationally adiabatic mixed quantum-classical trajectories are plotted in the solvent coordinate and reaction complex center-of-mass to illustrate the mechanisms observed for the phenol-amine proton transfer ( $R_{O-N} = 2.7$  Å) in confined  $\text{CH}_3\text{Cl}$  ( $R_{\text{cav}} = 10$  Å). Left: The solvent reorganizes first and is followed by motion of the reaction complex. Center: The reaction complex first moves into the cavity interior and is then followed by solvent reorganization. Right: The solvent reorganization and reaction complex motion occur in concert.

**TABLE 2: Percentage of Nonequilibrium Trajectories that Follow a Particular Pathway for Different Cavity Sizes and Hydrogen Bond ( $R_{\text{OH}}$ ) Distances<sup>a</sup>**

$R_{\text{cav}}$ (Å)	$R_{\text{OH}}$ (Å)	solvent coord.		solute pos.	
		first		first	nonreactive
10	2.6	75.8		24.2	45.0
10	2.7	87.0		12.9	5.5
10	2.8	92.5		7.5	0.0
12	2.6	72.6		27.4	20.1
12	2.7	89.0		11.0	4.4
12	2.8	89.8		10.2	1.6
15	2.6	68.0		32.0	16.6
15	2.7	79.5		20.4	2.2
15	2.8	85.3		14.6	3.3

<sup>a</sup> The results for the reaction mechanisms are given as a percentage of the reactive trajectories only. The percentage of all trajectories that are nonreactive are also given.<sup>63</sup> See the text for a discussion of the mechanism definitions and details of the assignment of the trajectories.

time. (This trajectory also exhibits a crossing of the dividing surface in the solvent coordinate at early times with a rapid return to reactants.)

As noted above, the trajectories can be complex, given the relatively low reaction barriers for the proton transfer systems considered here. To investigate the relative contributions of the different mechanisms, we have analyzed the individual trajectories. Specifically, the two degree-of-freedom trajectories, as shown in Figure 5, are assigned a mechanism by dividing the space into quadrants. The first quadrant represents the reactants and is defined by  $\Delta E < 0$  and  $R_c > R_{\text{div}}$  ( $R_{\text{div}} = R_{\text{cav}} - 5.5$  Å), where  $R_c$  is the distance of the reaction complex center-of-mass from the cavity center. (We have verified that the qualitative results are not sensitive to the precise choice of  $R_{\text{div}}$ , which is based on the solvent radial density presented and discussed below.) The second quadrant represents the metastable products near the cavity wall ( $\Delta E > 0$  and  $R_c > R_{\text{div}}$ ). The third quadrant represents the metastable reactants in the cavity interior ( $\Delta E < 0$  and  $R_c < R_{\text{div}}$ ). The final quadrant represents the products ( $\Delta E > 0$  and  $R_c < R_{\text{div}}$ ). To assign the mechanism, we focus on the last passage in the trajectory from reactants to products (every passage could be included, but in practice, there is only one or zero for the large majority of the trajectories) and map which quadrants are traversed on the way. This approach readily distinguishes between the two “stepwise” mechanisms discussed above at the expense of the concerted mechanism. However, we have found by inspection that the concerted mechanism occurs relatively rarely ( $\sim 1$ – $2$  trajectories out of 120 or 180). The results from this analysis are given in Table 2 and discussed in greater detail below. Generally, these data indicate that (1) the contribution of the mechanism in which the solute moves

first increases as the cavity size is increased, and (2) the same mechanism has a smaller contribution as the heavy atom distance,  $R_{O-N}$ , is increased.

**5.2. Cavity Size Effects.** The size of the cavity confining the methyl chloride solution affects several aspects of the proton transfer reaction dynamics including the reaction free energy, the reaction rate constant, and the contributions of the different mechanisms. A number of these effects have been noted above; here, we discuss them in greater detail.

We first consider the reaction free energy,  $\Delta G_{\text{rxn}}$ . It is immediately clear from the data presented in Table 1, obtained from fitting the nonequilibrium reactant populations in Figures 1–3 to eq 7, that  $\Delta G_{\text{rxn}}$  decreases (becomes more negative) as  $R_{\text{cav}}$  increases, i.e., the larger the cavity, the more exothermic the proton transfer reaction. We attribute this to an increase in the effective solvent polarity as the cavity size increases. Specifically, the ion pair products of the proton transfer reaction should be preferentially stabilized compared to the more neutral reactants as the effective solvent polarity is increased. This is consistent with previous studies on similar nanocavity systems. In particular, Senapati and Chandra calculated the dielectric constant of water in spherical hydrophobic nanocavities of different sizes.<sup>14</sup> They found that the dielectric constant increased (toward the bulk value) as the cavity radius was increased. In addition, we have previously observed that the fluorescence spectrum of a model dye molecule dissolved in confined methyl iodide and acetonitrile is shifted to lower energies for larger cavities;<sup>28</sup> the cavity model was the same as that used here. This shift in the fluorescence spectra was attributed to an increase in the effective solvent polarity, as the larger cavities contain a larger number of solvent molecules and constrain the solvent molecules less. Moreover, we found that the solvent polarity depends on position and that the solvent polarity in the cavity interior is more sensitive to cavity size than that near the wall. In the context of the proton transfer reaction considered here, this would suggest that the increase in reaction free energy is due primarily to stabilization of the ion pair products in the cavity interior.

The forward rate constant,  $k_f$ , also displays a distinct dependence on cavity size. In particular, for fixed  $R_{O-N}$ ,  $k_f$  increases with  $R_{\text{cav}}$  (see Table 1). That is, the proton transfer reaction is accelerated as the cavity size is increased. In addition, there is clearly a strong correlation between the rate constant and the reaction free energy which, as discussed in the previous paragraph, decreases as the cavity radius is increased. This relationship is illustrated in Figure 6 where  $-k_B T \ln\{k_f/(k_B T/h)\}$  is plotted versus  $\Delta G_{\text{rxn}}$ . Plotting the forward rate constant in this way gives an estimate of the relative free energy barriers for reaction. Thus, this plot is a crude approach for looking at

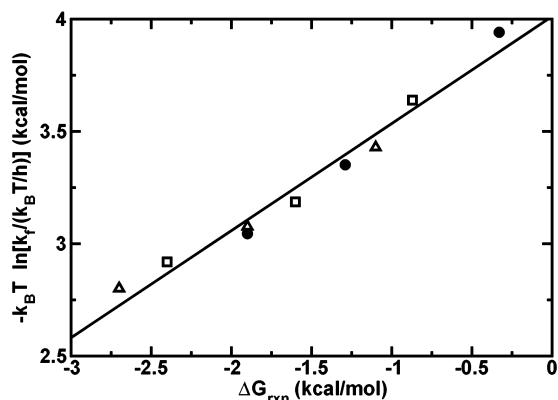


**Figure 6.** The forward proton transfer rate constant is plotted as  $-k_B T \ln\{k_f/(k_B T/h)\}$  vs the reaction free energy,  $\Delta G_{\text{rxn}}$ , for all the cavity sizes and heavy atom distances considered. The data for  $R_{\text{cav}} = 10$  Å (circles), 12 Å (squares), and 15 Å (triangles) are shown along with a linear fit to all the data (solid line).

the free energy relationship for these nanoconfined solvent systems (i.e., the connection between  $\Delta G^\ddagger$  and  $\Delta G_{\text{rxn}}$ ). We can see from this figure that the free energy barrier decreases as the reaction becomes more exothermic (either by increasing the cavity size or  $R_{\text{O-N}}$ ). The data are fairly well fit by a straight line with a slope (or Brønsted coefficient) of 0.48, though there appears to be a slight upward curvature which is discussed below. It is interesting to note that the correlation between  $k_f$  and  $\Delta G_{\text{rxn}}$  is consistent across the different cavity sizes and heavy atom distances.

As noted above, multiple mechanisms for the proton transfer reaction are observed, and the general effect of enlarging the cavity is to increase the occurrence of the minor pathway in which the solute diffuses into the cavity interior before the solvent reorganizes (see Table 2). The competition between the two primary mechanisms (ignoring for the present the rarer concerted mechanism) is naturally determined by the barrier for solvent reorganization near the cavity wall and the barrier for reactant motion into the cavity interior. Our previous Monte Carlo results found that the free energy barrier for solvent reorganization near the cavity wall is not strongly affected by cavity size,<sup>30</sup> though the favorable drop in free energy upon subsequent diffusion of the products into the cavity interior is more dramatically modified and increases with cavity radius.<sup>28</sup> On the other hand, the barrier for reactant diffusion to the cavity interior does decrease for larger cavities. Specifically, this barrier is directly related to the layered structure in the solvent radial density, which is more sharply peaked when the cavity size decreases. This layered structure and the cavity size dependence are shown in Figure 7 in which the total solvent radial density is plotted for  $R_{\text{cav}} = 10, 12$ , and 15 Å. It is clear from these results that the intensity of the solvent layering is reduced as the cavity radius is increased. This is naturally a reflection of the increasing severity of the constraints imposed by the confinement as the cavity is made smaller.

It appears that the data as shown in Figure 6 is reasonably represented by a linear free energy relationship,  $\Delta G^\ddagger = \alpha \Delta G_{\text{rxn}} + \Delta G_0^\ddagger$ , where  $\alpha$  is the Brønsted coefficient and  $\Delta G_0^\ddagger$  is the intrinsic free energy barrier.<sup>59</sup> However, as noted above, there appears to be a slight upward curvature in the data in Figure 6, implying that a nonlinear free energy relationship may be more appropriate. Nonlinearity in the free energy relationship can have a number of origins. For electron and proton transfer reac-

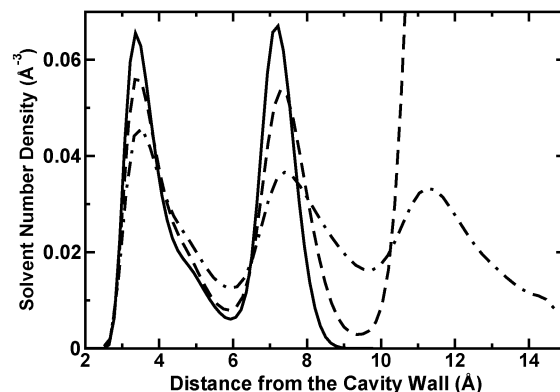


**Figure 7.** The solvent radial number density (summed over all atoms) obtained from Monte Carlo simulations is plotted as a function of the distance from the cavity wall for  $\text{CH}_3\text{Cl}$  in hydrophobic spherical nanocavities. Results are shown for  $R_{\text{cav}} = 10$  Å (solid line), 12 Å (dashed line),<sup>58</sup> and 15 Å (dot-dashed line). The details of the Monte Carlo simulations are given in ref 30.

tions, the nonlinear free energy relationship is expected to be<sup>44,59,60</sup>

$$\Delta G^\ddagger = \Delta G_0^\ddagger + \frac{\Delta G_{\text{rxn}}}{2} + \frac{\Delta G_{\text{rxn}}^2}{16\Delta G_0^\ddagger} \quad (13)$$

Fitting the present data to this equation does not provide a fit that is significantly better than the linear relation (i.e.,  $1/(16\Delta G_0^\ddagger)$  is small). A nonlinear free energy relationship can also arise when a reaction involves more than one barrier.<sup>61</sup> Fitting to a more general nonlinear free energy relation

$$\Delta G^\ddagger = \Delta G_0^\ddagger + \alpha \Delta G_{\text{rxn}} + \frac{1}{2} \alpha' \Delta G_{\text{rxn}}^2 \quad (14)$$

works well and yields  $\alpha = 0.80$  and  $\alpha' = 0.21$ .<sup>62</sup> Thus, it is tempting to speculate that the apparent curvature of the data in Figure 6 is due to changes in the relative contributions of the two primary mechanisms as the cavity size is changed. In particular, it might be attributable to the increasing barrier for reactant diffusion into the cavity interior as  $R_{\text{cav}}$  is decreased, which leads to an increase in the apparent overall free energy barrier for reaction (giving the upward curvature). However, this slight curvature is not dramatic, and we cannot eliminate uncertainties in the data as an origin of the curvature. A more definitive determination of the nonlinear free energy relationships in these systems will require further study.

**5.3. Heavy Atom Distance Effects.** In addition to changing the cavity size, we have explored the effect of varying the heavy atom distance,  $R_{\text{O-N}}$ . It is immediately clear from the data in Table 1 that  $\Delta G_{\text{rxn}}$  decreases (becomes more negative) as  $R_{\text{O-N}}$  increases. As noted above, we attribute this to the increased dipole moment of the products as the heavy atom distance is increased. In particular, the greater separation of the highly charged species in the ion pair product complex leads to better solvation by the polar methyl chloride solvent. In this sense, the  $\text{O} \cdots \text{N}$  distance serves to effectively adjust the reaction exothermicity in these systems. (This trend is naturally consistent with what would be observed in a bulk solution.) In concert with this change in the reaction free energy as  $R_{\text{O-N}}$  is increased, the forward rate constant increases, as shown in Table 1 and Figure 6.

The increased dipole moment of the product complex as the heavy atom distance is lengthened also affects the relative contributions of the two primary mechanisms (see Table 2).

Specifically, increasing  $R_{O-N}$  lowers the energy required to form the products near the cavity wall (via solvent reorganization), thereby enhancing the contribution of the mechanism in which the solvent reorganization precedes reaction complex motion. Since the charges in the reactant complex are comparatively small, increasing  $R_{O-N}$  does not greatly change the barrier for reactant diffusion into the cavity interior. Note that, not surprisingly, this change in the relative contributions of the two mechanisms is also correlated with the reduction in nonreactive trajectories (i.e.,  $\Delta G_{rxn}$  decreases as  $R_{O-N}$  increases as shown in Table 1).

## 6. Conclusions

We have used vibrationally adiabatic mixed quantum–classical molecular dynamics to simulate the proton transfer reaction in a model phenol–amine system dissolved in nanoconfined methyl chloride. The solution was confined in a spherical hydrophobic cavity, and the effect of varying the cavity radius was examined. In addition, the O–N hydrogen bond distance in the acid–base pair was fixed, and the effect of changing that heavy atom distance was investigated. Non-equilibrium vibrationally adiabatic mixed quantum–classical molecular dynamics simulations were used to calculate the time-dependent reactant population. Fitting this population to the solution of the appropriate kinetic equations gave the reaction free energies and rate constants.

The results show that the reaction free energies decrease (the reaction becomes more exothermic), and the rate constants increase as the cavity is made larger. This was attributed to an increase in the effective solvent polarity as the cavity size is increased. It was also found that the reaction free energies decrease and the rate constants increase as the O–N heavy atom distance is lengthened. This is attributed to the increased dipole moment of the ion pair product complex as  $R_{O-N}$  is elongated. This leads to better solvation of the products compared to the reactants, thereby decreasing  $\Delta G_{rxn}$ .

The mechanism of the proton transfer reaction was also considered. On the basis of the results of previous Monte Carlo simulations (which indicated that reaction complex position is part of the reaction coordinate), it was expected that three possible mechanisms might be observed. Specifically, the reaction must involve both solvent reorganization (as in a proton transfer reaction in bulk solvent) and motion of the reaction complex from near the wall (where reactants are favored) to the cavity interior (where products are favored). These can occur with solvent reorganization preceding the complex motion, reactant complex motion into the cavity interior preceding solvent reorganization, or concerted complex motion and solvent reorganization. In the present simulations, all three mechanisms are observed. The concerted pathway occurs relatively rarely. The dominant pathway involves solvent reorganization followed by diffusion of the nascent products into the cavity interior. However, the relative contribution of the two major pathways depends on both cavity size and O–N distance. Specifically, the mechanism in which reactant complex motion into the cavity interior precedes solvent reorganization becomes more prevalent as the cavity size is increased. This is attributed to the changes in the layered solvent density. This same mechanism becomes less prevalent as the heavy atom distance is increased for fixed cavity size. This is attributed to better solvation of the product complex as  $R_{O-N}$  is increased in the polar methyl chloride solvent.

The effect of including vibrationally nonadiabatic transitions in the rate constants and mechanism is an important issue that

will be addressed elsewhere. In addition, we are also studying analogous intermolecular proton transfer reactions to understand the role of the heavy atom distance when it is not constrained.

**Acknowledgment.** The author thanks Prof. Richard L. Schowen for useful discussions. This work was supported by the Chemical Sciences, Geosciences and Biosciences Division, Office of Basic Energy Sciences, Office of Science, U.S. Department of Energy.

## References and Notes

- (1) Brinker, C. J.; Scherer, G. W. *Sol–Gel Science: The Physics and Chemistry of Sol–Gel Processing*; Academic Press: New York, 1990.
- (2) MacGillivray, L. R.; Atwood, J. L. *Adv. Supramol. Chem.* **2000**, 6, 157–183. MacGillivray, L. R.; Atwood, J. L. *J. Solid State Chem.* **2000**, 152, 199–210. Atwood, J. L.; Barbour, L. J.; Ness, T. J.; Raston, C. L.; Raston, P. L. *J. Am. Chem. Soc.* **2001**, 123, 7192–7193. Cave, G. W. V.; Antesberger, J.; Barbour, L. J.; McKinlay, R. M.; Atwood, J. L. *Angew. Chem., Int. Ed.* **2004**, 43, 5263–5266. Steed, J. W.; Atwood, J. L. *Supramolecular Chemistry*; Wiley: New York, 2000.
- (3) Rebek, J., Jr. *Acc. Chem. Res.* **1999**, 32, 278–286. Gissot, A.; Rebek, J., Jr. *J. Am. Chem. Soc.* **2004**, 126, 7424–7425. Amaya, T.; Rebek, J., Jr. *J. Am. Chem. Soc.* **2004**, 126, 14149–14156. Palmer, L. C.; Rebek, J., Jr. *Org. Biomol. Chem.* **2004**, 2, 3051–3059.
- (4) Avram, L.; Cohen, Y. *J. Am. Chem. Soc.* **2004**, 126, 11556–11563. Kaanumalle, L. S.; Gibb, C. L. D.; Gibb, B. C.; Ramamurthy, V. *J. Am. Chem. Soc.* **2004**, 126, 14366–14367.
- (5) See, e.g., Fendler, J. H. *J. Phys. Chem.* **1980**, 84, 1485–1491 and Pileni, M. P., Ed. *Structure and Reactivity in Reverse Micelles*; Elsevier: New York, 1989.
- (6) See, e.g., Gu, L.-Q.; Cheley, S.; Bayley, H. *Science* **2001**, 291, 636–640.
- (7) Ping, G.; Yuan, J. M.; Vallieres, M.; Dong, H.; Sun, Z.; Wei, Y.; Li, F. Y.; Lin, S. H. *J. Chem. Phys.* **2003**, 118, 8042–8048. Friedel, M.; Sheeler, D. J.; Shea, J.-E. *J. Chem. Phys.* **2003**, 118, 8106–8113.
- (8) Brown, D.; Clarke, J. H. R. *J. Phys. Chem.* **1988**, 92, 2881–2888.
- (9) Linse, P. *J. Chem. Phys.* **1989**, 90, 4992–5004. Linse, P.; Halle, B. *Mol. Phys.* **1989**, 67, 537–573.
- (10) Zhang, J.; Jonas, J. *J. Phys. Chem.* **1993**, 97, 8812–8815. Korb, J.-P.; Xu, S.; Jonas, J. *J. Chem. Phys.* **1993**, 98, 2411–2422. Korb, J.-P.; Malier, L.; Cros, F.; Xu, S.; Jonas, J. *Phys. Rev. Lett.* **1996**, 77, 2312–2315. Korb, J.-P.; Xu, S.; Cros, F.; Malier, L.; Jonas, J. *J. Chem. Phys.* **1997**, 107, 4044–4050.
- (11) Loughnane, B. J.; Fourkas, J. T. *J. Phys. Chem. B* **1998**, 102, 10288–10294. Loughnane, B. J.; Scodinu, A.; Fourkas, J. T. *J. Phys. Chem. B* **1999**, 103, 6061–6068. Loughnane, B. J.; Farrer, R. A.; Scodinu, A.; Reilly, T.; Fourkas, J. T. *J. Phys. Chem. B* **2000**, 104, 5421–5429. Farrer, R. A.; Fourkas, J. T. *Acc. Chem. Res.* **2003**, 36, 605–612.
- (12) Tobias, D. J.; Klein, M. L. *J. Phys. Chem.* **1996**, 100, 6637–6648.
- (13) Senapati, S.; Keiper, J. S.; DeSimone, J. M.; Wignall, G. D.; Melnichenko, Y. B.; Frielinghaus, H.; Berkowitz, M. L. *Langmuir* **2002**, 18, 7371–7376. Senapati, S.; Berkowitz, M. L. *J. Chem. Phys.* **2003**, 118, 1937–1944. Senapati, S.; Berkowitz, M. L. *J. Phys. Chem. B* **2003**, 107, 12906–12916.
- (14) Senapati, S.; Chandra, A. *J. Phys. Chem. B* **2001**, 105, 5106–5109.
- (15) Turner, C. H.; Brennan, J. K.; Johnson, J. K.; Gubbins, K. E. *J. Chem. Phys.* **2002**, 116, 2138–2148.
- (16) Streck, C.; Melnichenko, Y. B.; Richert, R. *Phys. Rev. B* **1996**, 53, 5341–5347. Richert, R. *Phys. Rev. B* **1996**, 54, 15762–15766.
- (17) Riter, R. E.; Willard, D. M.; Levinger, N. E. *J. Phys. Chem. B* **1998**, 102, 2705–2714. Pant, D.; Riter, R. E.; Levinger, N. E. *J. Chem. Phys.* **1998**, 109, 9995–10003. Riter, R. E.; Undiks, E. P.; Kimmel, J. R.; Levinger, N. E. *J. Phys. Chem. B* **1998**, 102, 7931–7938. Willard, D. M.; Riter, R. E.; Levinger, N. E. *J. Am. Chem. Soc.* **1998**, 120, 4151–4160. Willard, D. M.; Levinger, N. E. *J. Phys. Chem. B* **2000**, 104, 11075–11080. Pant, D.; Levinger, N. E. *Langmuir* **2000**, 16, 10123–10130. Riter, R. E.; Undiks, E. P.; Levinger, N. E. *J. Am. Chem. Soc.* **1998**, 120, 6062–6067. Riter, R. E.; Kimmel, J. R.; Undiks, E. P.; Levinger, N. E. *J. Phys. Chem. B* **1997**, 101, 8292–8297.
- (18) Pal, S. K.; Sukul, D.; Mandal, D.; Sen, S.; Bhattacharyya, K. *J. Phys. Chem. B* **2000**, 104, 2613–2616.
- (19) Sarkar, N.; Das, K.; Datta, A.; Das, S.; Bhattacharyya, K. *J. Phys. Chem.* **1996**, 100, 10523–10527.
- (20) Bhattacharyya, K.; Bagchi, B. *J. Phys. Chem. A* **2000**, 104, 10603–10613.
- (21) Nandi, N.; Bagchi, B. *J. Phys. Chem.* **1996**, 100, 13914–13919.
- (22) Baumann, R.; Ferrante, C.; Deeg, F. W.; Bräuchle, C. *J. Chem. Phys.* **2001**, 114, 5781–5791. Baumann, R.; Ferrante, C.; Kneuper, E.; Deeg, F. W.; Bräuchle, C. *J. Phys. Chem. A* **2003**, 107, 2422–2430.
- (23) Zhang, J.; Bright, F. V. *J. Phys. Chem.* **1991**, 95, 7900–7907.



- (24) Hazra, P.; Sarkar, N. *Chem. Phys. Lett.* **2001**, *342*, 303–311.
- (25) Senapati, S.; Chandra, A. *J. Chem. Phys.* **1999**, *111*, 1223–1230.
- (26) Faeder, J.; Ladanyi, B. M. *J. Phys. Chem. B* **2000**, *104*, 1033–1046.
- (27) Faeder, J.; Ladanyi, B. M. *J. Phys. Chem. B* **2001**, *105*, 11148–11158.
- (28) Laria, D.; Kapral, R. *J. Chem. Phys.* **2002**, *117*, 7712–7718.
- (29) Thompson, W. H. *J. Chem. Phys.* **2002**, *117*, 6618–6628.
- (30) Thompson, W. H. *J. Chem. Phys.* **2004**, *120*, 8125–8133.
- (31) Thompson, W. H. *J. Phys. Chem. B* **2004**, *108*, 20144–20154.
- (32) Li, S.; Thompson, W. H. *J. Phys. Chem. B* **2005**, *109*, 4941–4946.
- (33) Eyal, M.; Reisfeld, R.; Chernyak, V.; Kaczmarek, L.; Grabowska, A. *Chem. Phys. Lett.* **1991**, *176*, 531–535.
- (34) McKiernan, J.; Simoni, E.; Dunn, B.; Zink, J. I. *J. Phys. Chem.* **1994**, *98*, 1006–1009.
- (35) Dunn, B.; Zink, J. I. *Chem. Mater.* **1997**, *9*, 2280–2291.
- (36) Proposito, P.; Marks, D.; Zhang, H.; Glasbeek, M. *J. Phys. Chem. A* **1998**, *102*, 8894–8902.
- (37) Proposito, P.; Marks, D.; Zhang, H.; Glasbeek, M. *Radiat. Eff. Defects Solids* **1999**, *150*, 385–389.
- (38) Nogami, M.; Nagao, R.; Cong, W.; Abe, Y. *J. Sol.-Gel Sci. Technol.* **1998**, *13*, 933–936.
- (39) Nogami, M. *J. Sol.-Gel Sci. Technol.* **2004**, *31*, 359–364.
- (40) Daiko, Y.; Kasuga, T.; Nogami, M. *Micropor. Mesopor. Mater.* **2004**, *69*, 149–155.
- (41) Carturan, S.; Quaranta, A.; Maggioni, G.; Vomiero, A.; Ceccato, R.; Della Mea, G. *J. Sol.-Gel Sci. Technol.* **2003**, *26*, 931–935.
- (42) Carturan, S.; Maggioni, G.; Ceccato, R.; Della Mea, G. *J. Non-Cryst. Solids* **2003**, *322*, 1–6.
- (43) Cohen, B.; Huppert, D.; Solntsev, K. M.; Tsfadia, Y.; Nachliel, E.; Gutman, M. *J. Am. Chem. Soc.* **2002**, *124*, 7539–7547.
- (44) Umoto, H.; Abe, K.; Kawasaki, C.; Igarashi, T.; Sakurai, T. *J. Photochem. Photobiol., A* **2003**, *156*, 127–137.
- (45) Kwon, O.-H.; Jang, D.-J. *J. Phys. Chem. B* **2005**, *109*, 8049–8052.
- (46) Das, S.; Datta, A.; Bhattacharyya, K. *J. Phys. Chem. A* **1997**, *101*, 3299–3304.
- (47) Mandal, D.; Pal, S. K.; Bhattacharyya, K. *J. Phys. Chem. A* **1998**, *102*, 9710–9714.
- (48) Pal, S. K.; Mandal, D.; Bhattacharyya, K. *J. Phys. Chem. B* **1998**, *102*, 11017–11023.
- (49) Bardez, E.; Goguillon, B.-T.; Keh, E.; Valeur, B. *J. Phys. Chem.* **1984**, *88*, 1909–1913.
- (50) Bardez, E.; Monnier, E.; Valeur, B. *J. Phys. Chem.* **1985**, *89*, 5031–5036.
- (51) Valeur, B.; Bardez, E. In *Structure and Reactivity in Reverse Micelles*; Pileni, M. P., Ed.; Elsevier: New York, 1989.
- (52) Politi, M. J.; Chaimovich, H. *J. Phys. Chem.* **1986**, *90*, 282–287.
- (53) Marcus, R. A. *Annu. Rev. Phys. Chem.* **1964**, *15*, 155–196.
- (54) Newton, M. D.; Sutin, N. *Annu. Rev. Phys. Chem.* **1984**, *35*, 437–480.
- (55) See, e.g.: Marcus, R. A. *Proc. Electrochem. Soc.* **1980**, *80*, 1–14.
- (56) Juanós i Timoneda, J.; Hynes, J. T. *J. Phys. Chem.* **1991**, *95*, 10431–10442.
- (57) Geissler, P. L.; Dellago, C.; Chandler, D.; Hutter, J.; Parrinello, M. *Science* **2001**, *291*, 2121–2124.
- (58) Warshel, A. *Computer Modelling of Chemical Reactions in Proteins and Solution*; Wiley: New York, 1991.
- (59) Aqvist, J.; Warshel, A. *Chem. Rev.* **1993**, *93*, 2523–2544.
- (60) Azzouz, H.; Borgis, D. *J. Chem. Phys.* **1993**, *98*, 7361–7375.
- (61) Azzouz, H.; Borgis, D. *J. Mol. Liq.* **1995**, *63*, 89–107.
- (62) Hammes-Schiffer, S.; Tully, J. C. *J. Chem. Phys.* **1994**, *101*, 4567–4667.
- (63) Staib, A.; Borgis, D.; Hynes, J. T. *J. Chem. Phys.* **1995**, *102*, 2487–2505.
- (64) Bigot, B.; Costa-Cabral, B. J.; Rivail, J. L. *J. Chem. Phys.* **1985**, *83*, 3083–3094.
- (65) The volume used in calculating this density is obtained by reducing the nominal cavity radius by  $0.5\sigma_{\text{wall}}$  ( $\sigma_{\text{wall}}$  is the effective Lennard-Jones radius of the cavity wall) to approximately account for the excluded volume, a quantity that changes significantly with cavity size.
- (66) Borgis, D.; Tarjus, G.; Azzouz, H. *J. Phys. Chem.* **1992**, *96*, 3188–3191.
- (67) Borgis, D.; Tarjus, G.; Azzouz, H. *J. Chem. Phys.* **1992**, *97*, 390–400.
- (68) Laria, D.; Ciccotti, G.; Ferrario, M.; Kapral, R. *J. Chem. Phys.* **1992**, *97*, 378–388.
- (69) Colbert, D. T.; Miller, W. H. *J. Chem. Phys.* **1992**, *96*, 1982–1991.
- (70) Lanczos, C. *J. Res. Natl. Bur. Stand. (U.S.)* **1950**, *45*, 255–282.
- (71) Thompson, W. H. *J. Chem. Phys.* **2003**, *118*, 1059–1067.
- (72) Bond, S. D.; Leimkuhler, B. J.; Laird, B. B. *J. Comput. Phys.* **1999**, *151*, 114–134.
- (73) Steinfeld, J. I.; Francisco, J. S.; Hase, W. L. *Chemical Kinetics and Dynamics*; Prentice Hall: Englewood Cliffs, NJ, 1989.
- (74) Another choice would be to calculate the reactant population using a dividing surface in the proton coordinate (here, the proton expectation value). We have found that the reactant population defined in this way is identical to that obtained using a dividing surface in the solvent coordinate, eq 8. That is, the proton position fully tracks the solvent coordinate.
- (75) The extremely high-density peak for  $R_{\text{cav}} = 12 \text{ \AA}$  at  $\sim 11\text{--}12 \text{ \AA}$  from the cavity wall is due to a single solvent molecule located in the center of the cavity. The small volumes of the histogram bins nearest the cavity center give the very large densities.
- (76) Marcus, R. A. *J. Phys. Chem.* **1968**, *72*, 891–898.
- (77) Cohen, A. O.; Marcus, R. A. *J. Phys. Chem.* **1968**, *72*, 4249–4256.
- (78) Marcus, R. A. *J. Am. Chem. Soc.* **1969**, *91*, 7224–7225.
- (79) Kiefer, P. M.; Hynes, J. T. *J. Phys. Chem. A* **2002**, *106*, 1834–1849; 1850–1861.
- (80) See, e.g., Carroll, F. A. *Perspectives on Structure and Mechanism in Organic Chemistry*; Brooks/Cole: Pacific Grove, CA, 1998.
- (81) We have also tried fitting to  $k_{\text{f}} = k_1 + k_2$  (i.e., assuming two pathways with different rate constants contribute to  $k_{\text{f}}$ ) where  $k_i = (k_{\text{B}}T/h) \exp(-\Delta G_i^\ddagger/k_{\text{B}}T)$  and  $\Delta G_{\text{f}}^\ddagger = \Delta G_{0,i}^\ddagger + \alpha_i \Delta G_{\text{rxn}}$ . We were unable to obtain a reasonable fit in which  $k_1$  and  $k_2$  contributed. An accurate fit of this form likely requires more extensive data than presented in Figure 6.
- (82) Note that the percentage of nonreactive trajectories does not (and should not be expected to) precisely correspond to the equilibrium reactant populations given in Table 1. The equilibrium populations are obtained by fitting the time-dependent reaction population rather than counting trajectories, and those populations (unlike the percentages in Table 2) are based on only the solvent coordinate value.